https://cimav.repositorioinstitucional.mx/jspui

Giant Magnetization on Mn3Ga Ultra-Thin films grown by Magnetron Sputtering on SiO_2/Si(001)

R. M. Gutiérrez-Pérez, J. T. Holguín-Momaca, J. T. Elizalde-Galindo, F. Espinosa-Magaña, and S. F. Olive- Méndez

Abstract

Mn3Ga films were grown by rf-sputtering on SiO_2/Si(001) substrates at 300 °C. Ultra-thin films with 2 nm of thickness are composed of small grains with an in-plane diameter ~27 nm. The film exhibits an out-of-plane saturation magnetization $M_s^{\perp}$=1690 emu/cm^3 (15 times the bulk magnetization value) and in-plane $M_s^{//}$=216 emu/cm^3, corresponding to 3.3 and 0.43$_{\mu B}$/Mn at. Giant magnetization is attributed to uncompensated Mn moments located at the intergrain boundaries. No surface anisotropy is expected due to the high anisotropy constant of Mn_3Ga. M_s decreases as the film thickness increases due to grain growth and subsequent decrease in intergrain boundary surface area. Magnetic M(H) loops remain anhysteretic for thickness ≤10 nm, corresponding to an average grain size <50 nm, suggesting that nanocrystals are magnetic monodomains. Films with thickness >10 nm exhibit coercivity between 9 and 19 kOe and M_s from 25 to 72 emu/cm^3 with a residual weak ferromagnetic component. Hysteretic M(H) loops are the signature of the existence of magnetic multidomain

grains with average grain size >50 nm. All films exhibit higher out-of- plane M_s than in-plane magnetization.

Introduction

Tetragonal s-Mn3Ga has attracted much attention due to the wide variety of technological applications ranging from substitution of rare-earth permanent magnets [1, 2, 3] with nanostructured $Mn_{3-x}Ga$ to spintronics applications using epitaxial thin films [4, 5]. This phase has the Al_3Ti-type ($D0_{22}$ space group I4/mmm) crystal structure and exhibits a ferrimagnetic (FiM) coupling along *c* axis [6]. This FiM order is produced by the interatomic separation of two different Mn positions, namely, Mn_I and Mn_{II} atoms, which nearest neighbor atomic separation is 2.56 Å. Mn atom separation between 250 and 280 pm leads to antiferromagnetic coupling, while distances 290 pm are needed to achieve ferromagnetic (FM) coupling [7] τ-Mn_3Ga has large coercivity, low saturation magnetization (M_s), high crystal anisotropy, high Curie temperature T_C=770 K, and spin polarization of 58%. This particular combination of magnetic properties ensures the stability of the magnetic orientation of the free layer in a magnetic tunnel junction (MTJ), against external magnetic fields or thermal perturbation.

Moreover, these magnetic properties can be tuned by modifying the Mn amount on the formula Mn_xGa with x=3 - 0.33. A few examples are: epitaxial Mn_2Ga/MgO(001) films exhibit an out-of-plane $M_s^{\perp}$=470 emu/cm^3 and K1=2.35 x 10^7 erg/cm^3, while Mn_3Ga has $M_s^{\perp}$=110 emu/cm^3 and K_1=0.89*10^7 erg/cm^3 [8]. This higher magnetization but lower

spin polarization (40%) makes Mn_2Ga suitable for high-density memory storage devices. Moreover, $Mn_{2.5}Ga$ films exhibit intermediate M_s and K_1 values compared to that of Mn_2Ga and Mn_3Ga [9]. Epitaxial MnGa films grown on GaN(111) exhibit two in-plane easy magnetization axis with M_s~650 emu/cm^3 and K_1=1.3*10^7 erg/cm^3 [10]. Finally, $MnGa_3$ films exhibit semiconductor behavior with a low content of $_{\varphi}$-$Ga_{7.7}Mn_{2.3}$, a Ga-rich phase [11].

The substrate selection is also important; Mn_3Ga films grown on GaSb(001) exhibit the planar Mn_3Ga(114)// GaSb(001) epitaxial relationship, the in-plane and out-of-plane M_s are both anhysteretic with almost the same M_s=400 emu/cm^3 [11]. Besides, it has been observed that 2x2 surface reconstruction on epitaxial $Mn_{1.2\text{-}1.5}Ga$/GaN(0001) films produces higher M_s and higher K1 than films showing 1x1 reconstruction [12]. Furthermore, Mn_3Ga has two additional crystal structures: cubic and hexagonal. The hexagonal $_{\varepsilon}$-Mn_3Ga is antiferromagnetic with a triangular spin structure and a weak ferromagnetic component below 460 K that can be eliminated by tensile strain [13]. This antiferromagnetic phase represents particular interest due to the possibility of exchange bias with $_{\tau}$-Mn_3Ga (i.e., pinning of the free layer on a MTJ) [14]. The cubic phase is paramagnetic and becomes ferrimagnetic under thermal treatment.

In this paper, we present the results on Mn_3Ga thin films with thicknesses from 2 to 50 nm. High nucleation rate at the initial growth stages produces high boundary

surface area producing giant saturation magnetization due to uncompensated spin at the surface of the nanocrystals.

Experimental details

Prior to film growth, a 2^{II}-Mn_3Ga target was fabricated using an induction oven and the stoichiometric amounts of Ga and Mn, both from Sigma-Aldrich and a purity of 99.9%. The materials were placed on a graphite crucible covered with Boron Nitride nanoparticles to avoid carbon diffusion into the target. The vacuum on the oven prevents oxidation from air. After melting, the target was polished to remove all carbon traces from the crucible. Characterization of the target by energy dispersive X-ray spectroscopy (EDS) shows a Mn composition of 73.8 at. % and 26.2 at. % for Ga, very close to 3:1 proportion on Mn_3Ga. The X-ray diffraction (XRD) pattern of the target was used for comparison with the XRD patterns of the obtained films. Furthermore, Rietveld analysis of the target, showed that 83 wt. % was $_{\tau}$-Mn_3Ga and 17 wt. %, corresponds to εMn_3Ga. In Fig. 1(b), the peaks at 40.5 and 44.5° correspond to the (002) and (110) crystallographic planes of the hexagonal phase.

Substrates were 2x2 cm^2 sections cut from an 8'' SiO_2/ Si(001) wafer. Sections were cleaned in ultrasonic bath for 10 min with trichloroethylene, acetone, and ethanol, and rinsed with tridistilled water after each solvent. Substrates were introduced into the growth chamber through a load lock pre-chamber. The sputtering system, from AJA International, model ATC ORION 5 UHV is equipped with 4–2'' magnetrons and 1–1''

magnetron, a thickness measuring system and a reflection high-energy electron diffraction (RHEED) equipment from STAIB, operating at 30 kV used to control surface crystal structure. The base pressure of the system is $2.4*10^{-8}$ Torr. Mn3Ga films were grown using a RF power source at 40 W corresponding to a growth rate of 2.9 nm/min, which was calibrated using scanning electron microscopy (SEM) for a 200 nm thick film deposited at 300 °C. The different thicknesses of the samples were obtained by fixing the growth time to obtain films of 2, 3.5, 5, 10, 20, and 50 nm. Structural characterization was performed using X-ray diffractometry in grazing incidence with a fixed incidence angle of 0.5° in a PANalytical X'Pert equipment. The surface morphology was studied using atomic force microscopy (AFM) using a Veeco SPM MultiMode equipment. High-resolution transmission electron microscopy (HR-TEM) in cross-sectional view was performed on some samples using a JEOL JEM 2200Fs+Cs. Samples were prepared in a focused-ion beam equipment from JEOL. The composition of the films was obtained by EDS analysis during TEM observations, using an Oxford spectrometer and INCA software for quantification. Magnetic in-plane and out-of-plane M(H) measurements were performed at room temperature using a Versalab magnetometer from Quantum Design.

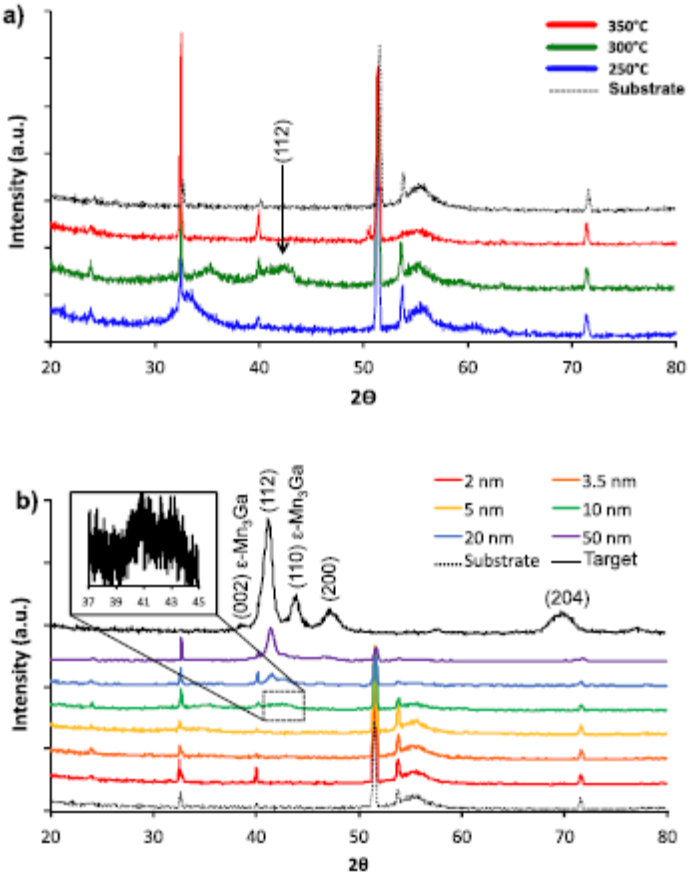

FIG. 1. XRD patterns of (a) 10 nm films grown at different temperatures; crystal quality is enhanced at $T_s = 300$ °C. (b) Samples with different thicknesses, diffraction of the tetragonal phase starts to be observed for thickness ≥ 10 nm. The inset in (b) is a long-time scan to show in detail the broad peak in sample with 10 nm in thickness.

Results and Discussion

Different substrate temperatures (T_s) were used in order to improve the crystal quality of the 10 nm thick films. The obtained XRD patterns of films grown at T_s=250, 300, and 350 °C are shown in Fig. 1(a). For comparison purposes, the XRD pattern of the bare SiO_2/Si(001) substrate was presented. Only at 300 °C, a feature between 40

and 45o was observed which corresponds to the (112) peak of the $_{T}$-Mn3Ga phase [15]. In Fig. 1(b), the evolution of the XRD patterns of the $_{T}$-Mn_3Ga films dependent on the thickness is shown. The volume of ultra-thin films ≤10 nm is too small compared with the bulk silicon substrate to be detectable by X-rays and to produce diffraction patterns. The inset in Fig. 1(b) is a long-time scan to evidence that the broad peak corresponds to two peaks at 40.87 and 42.5°. For films with thickness ≥10 nm, the most intense signal corresponds to the (112) peak at 41.2°. For the film with 50 nm in thickness, there is a shift to the left of the (112) peak indicating an interplanar tensile strain that must be compensated by a compressive strain in some other crystallographic direction. No peaks corresponding to the $_{\varepsilon}$-Mn3Ga phase, which may appear at 40.5, 44.5, and 69° were observed.

A powerful *in-situ* characterization technique is RHEED, which produces diffraction patterns of the surface of the film in real time along a selected azimuth. RHEED technique was used to follow the crystal evolution of the surface depending on the film thickness and temperature. A RHEED pattern of the bare SiO_2/Si(001) substrate is shown in Fig. 2(a), the 1x1 streaky pattern was obtained along [110] direction, which disappears progressively with Mn_3Ga deposition (Fig. 2(b)). In Fig. 2(c), a polycrystalline RHEED pattern formed by concentric rings corresponding to a polycrystalline ordered surface is shown, which appears for film thickness ≥13 nm. This pattern remains unchanged for thicker films. Thermal stability was tested for the 2 nm ultra- thin film by

heating the sample up to 550 °C, the RHEED pattern changes from a continuous background to a ring-like pattern at 550 °C as shown in Fig. 2(d), indicating that nanocrystals coalesce to form larger organized zones.

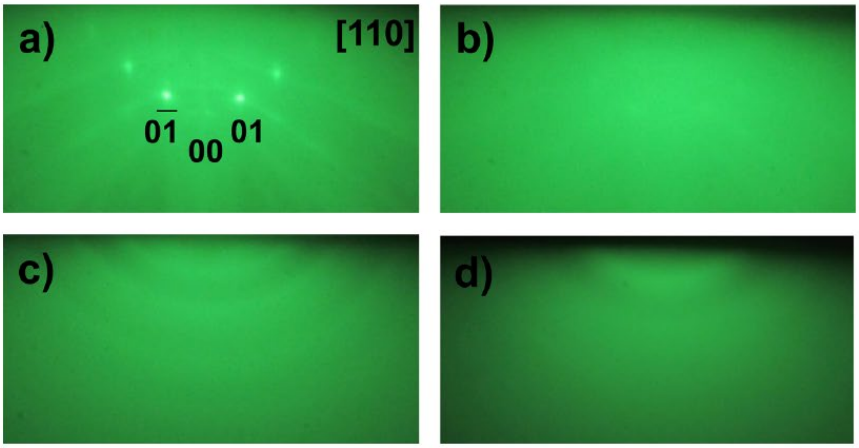

FIG. 2. RHEED patterns of the growth evolution of a Mn_3Ga film. (a) Bare SiO_2/Si(001) substrate along the [110] direction, (b) continuous background for sub-10 nm thin film, (c) polycrystalline ring-like pattern for thickness >13 nm, and (d) ring-like pattern for the 2 nm thick sample annealed at 550 °C.

The evolution of the surface morphology was studied by AFM scanning 1x1 μm^2 areas. AFM micrographs for films with 2 and 50 nm in thickness are shown in Figs. 3(a) and 3(b), respectively, the first one is constituted of grains with an average in-plane diameter of 27 nm that increases to 67 nm when film thickness increases to 50 nm. The low surface free energy σ=0.3 J/m^2 of SiO_2 does not favor a good adherence of add-atoms, then high nucleation rate followed by three-dimensional growth occurs at the initial growth stages. The second step is an in-plain grain growth combined with nanocrystal surface diffusion to form clusters of ~250 nm to minimize exposed surface area. Clusters are encircled in Fig. 3(b). A plot of the grain size and roughness against

film thickness is shown in Fig. 3(e). The evolution of grain size can be fitted with the expression for growth kinetics given by $G^n=k_{0t}$ exp (-Q/RT), where n is the kinetic grain growth exponent, k_0 is the pre-exponential factor, t is time, Q is the apparent activation energy, R is the gas constant, and T absolute temperature [16]. Fitting the experimental values of the average grain size with the above expression leads to n=3.33, meaning an in-plane high growth rate. In other words, for ultra thin films, deposition rate is 2.9 nm/s while radial grain growth is ~12.6 nm/min. The evolution of the roughness vs. thickness follows a linear approach, suggesting that equilibrium between maximum grain size and nucleation rate is not yet achieved for a 50 nm thin film. For a single grain, the in-plane growth rate is larger than the deposition rate assuming that Ostwald ripening mechanism governs grain growth. An AFM micrograph of the 2 nm ultra-thin film after thermal annealing at 550 °C is shown in Fig. 3(c), which exhibits larger grains than those observed before annealing. The line profiles of the insets on Figs. 3(a) and 3(c) are shown in Fig. 3(d), demonstrating the formation of larger zones. These areas are formed by coalescence leading to a significant reduction of the rms roughness from 3 to 0.3 nm.

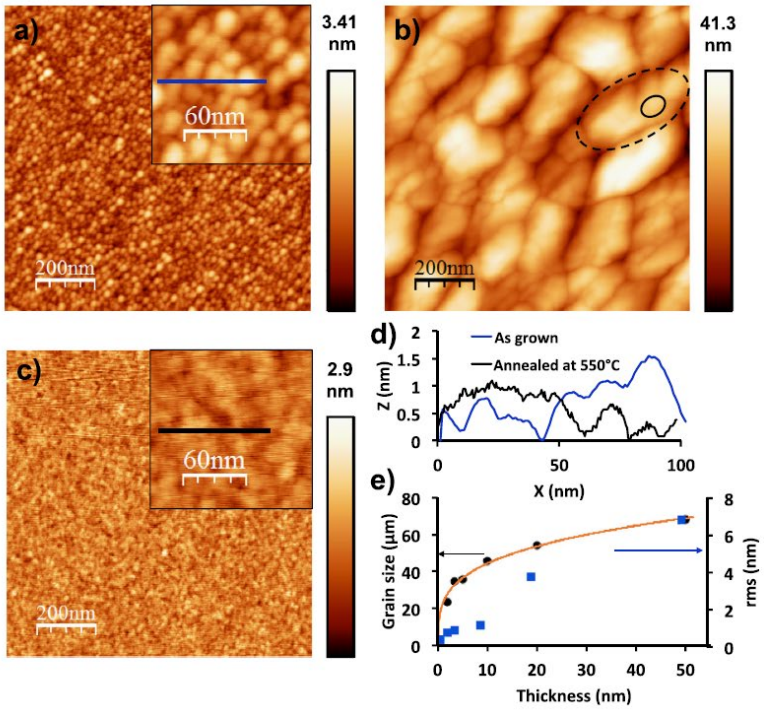

FIG. 3. AFM micrographs for samples with thickness (a) 2 nm, (b) 50 nm, and (c) 2 nm after annealing at 550 °C. (d) Line profile from the insets of panels (a) and (c) showing larger zones on the annealed sample compared to the grains of the 2 nm sample. (e) Grain size and roughness evolution vs thickness.

HR-TEM micrographs of films with 2 and 50 nm of thickness are shown in Figs. 4(a) and 4(c), where the thickness of both samples is confirmed. The interface with the cover Au layer is similar to the AFM line profile shown in Fig. 3(c) as film-growth is three-dimensional. For the 50 nm film, a low magnification TEM micrograph (Fig. 4(b)) shows that the film is constituted of large grains with an in-plane diameter 80 nm in agreement with AFM observations. On the HR-TEM micrograph shown in Fig. 4(c), one can observe large crystalline zones (confirming Ostwald ripening); the inset is a filtered image using fast Fourier transform of the selected area. Two interplanar distances were measured: 2.07 and 2.22 Å, identified as (112) and (100) Mn_3Ga planes, respectively.

The bulk interplanar distances for these planes are 2.05 and 2.18 Å implying that tensile strain is induced on the film along [100] and [111] directions, respectively (as mentioned before on the XRD analysis). A compensating compressive strain must be found along [021] direction, which is perpendicular to the plane of the micrograph. This planes form an angle of 66° compared to 62.2° in bulk, corresponding to a deformation of 3.8°. In the filtered zone, crystal twins are observed along [100] direction, where (100) planes switch 180° each eight (100) planes as indicated by the dotted line; this bi-dimensional defect probably appears to compensate the distorted angle between (112) and (100) planes. The chemical composition of the film was determined by EDS analysis during HR-TEM observations. The Mn concentration is slightly reduced on the film due to Mn diffusion towards the Au cover layer and to the Si substrate through the SiO2 layer. The final composition is $Mn_{2.76}Ga$. High Mn diffusivity has been also observed in Mn-Ge-based thin films [17].

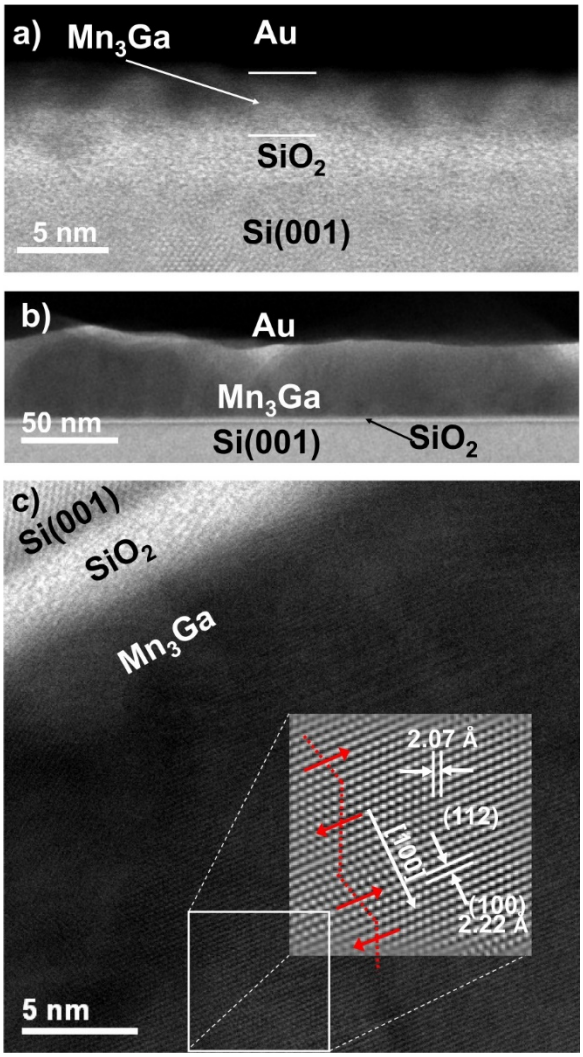

FIG. 4. TEM micrographs for (a) 2nm sample and (b) 50nm sample. (e) HR-TEM micrograph from (b). The interplanar distances indicate !ensile strain on the film.

In-plane (///) and out-of-plane ($\perp$) M(H) loops are shown in Fig. 5 for samples with thickness 2, 10, and 50 nm after subtraction of the substrate diamagnetic component. M(H) loops of ultra-thin films have a high noise-to-signal ratio originated from the

magnetometer resolution ($1*10^{-6}$ emu) as the dimensions of the sample are limited to 2x2 mm^2 to fit the sample holder. The experimental $M^{\perp}(H)$ loops have been corrected increasing each data point 5.5% as a geometrical factor of the difference between $M^{//}(H)$ and $M^{\perp}(H)$ measurements performed on pure Co thin films using the Versalab magnetometer. The 2 nm thin film has an in-plane saturation magnetization $M_s^{//}$=216 emu/cm^3 and a giant $M_s^{\perp}$=1690 emu/cm^3, which is ~15 times the bulk Mn3Ga magnetization (M_s=110 emu/cm^3) [18]. This giant $M_s^{\perp}$ is attributed to frustrated spin compensation at the surface of nanocrystals com- posing the film, no surface anisotropy is expected due to the high crystal anisotropy K_1 of $_{T}$-Mn_3Ga. The magnetic moments are $m^{\perp}$=3.3 and $m^{//}$=0.43$_{\mu B}$/Mn at. The high values of $m^{\perp}$ can only be understood if ferromagnetic order is established on the sample, in particular, at the shell of nanograins. Thickness increase is followed by grain growth implying a decrease in the intergrain surface area. For the 10 nm thin film (Fig. 5(b)), $M^{//}$=79 emu/cm^3 and $M_s^{\perp}$=260 emu/cm^3, which are still higher than bulk M_s. Epitaxial $_{T}$-Mn3Ga films also exhibit a FM component for measurements along the hard magnetization axis (in-plane measurement) attributed to frustrated spin compensation of the FiM order, with M_s=30 emu/cm^3 [19].

https://cimav.repositorioinstitucional.mx/jspui

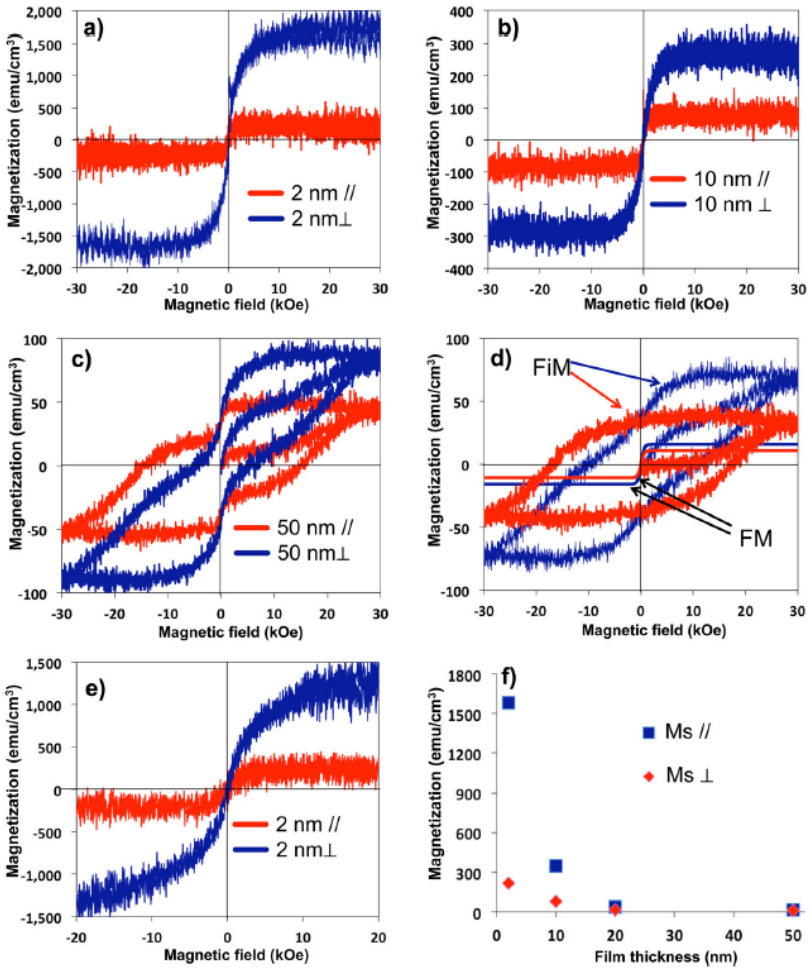

FIG. 5. In-plane $M^{//}(H)$ and out-of–plane $M^{\perp}(H)$ loops for samples (a) 2, (b) 10, and (c) 50 nm. Hysteretic M(H) loops are obtained for thickness ≥20 nm. (d) Separation of the FiM and FM components observed on (c). (a) and (e) Giant magnetization $M_s^{\perp} = 1690$ emu/cm^3 is obtained on 2 nm thick films, thermal treatment at 550 °C reduces $M_s^{\perp}$ to 1190 emu/cm^3. (f) Evolution on the intensity on the superparamagnetic component of the films vs film thickness.

TABLE I. Compilation of the data obtained in this paper compared to that of epitaxial thin films and bulk Mn_3Ga.

Thickness (nm)	$M_s^{//}$ [a] (emu/cm^3)	$M_s^{\perp}$ (emu/cm^3)	$H_c^{//}$ (kOe)	$H_c^{\perp}$ (kOe)	$FiM^{//}$ (emu/cm^3)	$FiM^{\perp}$ (emu/cm^3)
2	216	1690	…	…	…	…
10	79.2	345	…	…	…	…
20	14.4	36	16	19	25.2	28.8
50	10.8	15.8	16	9	36	72
Bulk ($Mn_{2.33}Ga$)	…	…	…	13.5	360	360
Epitaxial film	22	0	0	1.8	110	110

[a](FiM: ferrimagnetic and M_s: ferromagnetic saturation magnetization). Bulk values were obtained from Ref. 18 and epitaxial film values from Ref. 6.

The fact that $M_s^{\perp}$>$M^{//}$(H) for all samples suggests that the easy magnetization axis has its larger component perpendicular to the surface substrate. The anhysteretic feature of the M_s loops for films ≤10 nm suggests that grains are monodomain (average grain size ~47 nm). Hysteretic M(H) loops are obtained for thickness >20 nm, with average grain size ~60 nm, then a magnetic monodomain should have a size ≥50 nm. Our ultra thin-films are a combination of shell- ferromagnetism and core FiM-superparamagnetic solid system. Fig. 5(f) depicts the evolution of this anhysteretic component, which decreases with increasing thickness.

As demonstrated by XRD and HR-TEM experiments, in films with 20 and 50 nm of thickness, the crystal quality was improved and hysteretic M(H) loops are obtained despite that a FM signal persists (Figs. 5(c) and 5(d)). The FM component decreases as thickness increases reaching minimum values of 11 emu/cm^3. On the other hand, coercivity and remanence increase with film thickness (see Table I and Fig. 5(f)). For the 50 nm thin film $M_s^{\perp}$=72 emu/cm^3, close to 110 emu/cm^3 measured on epitaxial films [20]. The 2 nm thin film after thermal anneal treatment up to 550 ºC exhibits a reduction of $M_s^{\perp}$=1190 emu/cm^3 as shown in Fig. 5(e). It was previously demonstrated by AFM that an improvement of the roughness surface was obtained as well as an apparent increase in grain size; this magnetization reduction is then attributed to a reduction of the intergrain surface area.

https://cimav.repositorioinstitucional.mx/jspui

Conclusions

In this work, we present the giant magnetization of ultra-thin Mn_3Ga films grown by rf-magnetron sputtering on SiO_2/ Si(001) substrates. AFM microscopy was used to measure grain size evolution vs time, equation $G^n=k_{0t}\exp(-Q/kT)$ was used to find the grain growth exponent n=3.33 corresponding to an in-plane high grain growth rate for our experimental conditions. The in-plane and out-of plane anhysteretic M(H) loops show that sub-10 nm films are composed by magnetic monodomain grains. Ultra-thin film with 2 nm in thickness has a saturation magnetization $M_s^{\perp}$=1690 emu/cm^3, which is ~15 times the Mn_3Ga bulk magnetization, corresponding to a magnetic moment of $3.3\mu_B$/Mn atom. This giant value is attributed to uncompensated ferrimagnetic moments at the surface of Mn3Ga nanocrystals producing ferromagnetic order on the shell of the nanograin. Increasing film thickness produces larger grains which are magnetic multidomain that are at the origin of hysteretic M(H) loops. The ferromagnetic component decreases to 15.8 emu/cm^3 for a 50 nm thick film, at the same time that hysteretic feature and coercivity are observed.

Acknowledgements

The authors thank the financial support received from the Fondo Mixto Chihuahua FOMIX Grant No. CHIH-2011- C03-168831.

https://cimav.repositorioinstitucional.mx/jspui

References

1 J. M. D. Coey, J. Phys.: Condens. Matter 26, 064211 (2014).

2 M. E. Jamer, B. A. Assaf, S. P. Bennett, L. H. Lewis, and D. Heiman, J. Magn. Magn. Mater. 358–359, 259 (2014).

3 T. J. Nummy, S. P. Bennett, T. Cardinal, and D. Heiman, Appl. Phys. Lett. 99, 252506 (2011).

4 M. Glas, D. Ebke, I.-M. Imorz, P. Thomas, and G. Reiss, J. Magn. Magn. Mater. 333, 134 (2013).

5 W. Feng, Y. Shin, S. Cho, and D.-D. Dung, J. Korean Phys. Soc. 63, 1055 (2013).

6 H. Kurt, K. Rode, M. Venkatesan, P. Stamenov, and J. M. D. Coey, Phys. Rev. B 83, 020405(R) (2011).

7 N. Yamada, J. Phys. Soc. Jpn. 59, 273 (1990).

8 H. Kurt, K. Rode, M. Venkatesan, P. Stamenov, and J. M. D. Coey, Phys. Status Solidi B 248, 2338 (2011).

9 K. Rode, N. Baadji, D. Betto, Y.-C. Lau, H. Kurt, M. Venkatesan, P. Stamenov, S. Sanvito, and J. M. D. Coey, Phys. Rev. B 87, 184429 (2013).

10 A. W. Arins, H. F. Jurca, J. Zarpellon, J. Varalda, I. L. Graff, A. J. A. de Oliveira, W. H. Schreiner, and D. H. Mosca, Appl. Phys. Lett. 102, 2408 (2013).

11 W. Feng, D. Duc Dung, Y. Shin, D. Van Thiet, S. Cho, and X. Hao, J. Korean Phys. Soc. 56, 1382 (2010).

12 E. Lu, D. C. Ingram, A. R. Smith, J. W. Knepper, and F. Y. Yang, Phys. Rev. Lett. 97, 146101 (2006).

13 H. Niida, T. Hori, and Y. Nakagawa, J. Phys. Soc. Jpn. 52, 1512 (1983).

14 H. Kurt, K. Rode, H. Tokuc, P. Stamenov, M. Venkatesan, and J. M. D. Coey, Appl. Phys. Lett. 101, 232402 (2012).

15 P. Kharel, Y. Huh, N. Al-Aqtash, V. R. Shah, R. F. Sabirianov, R. Skomski, and D. J. Sellmyer, J. Phys.: Condens. Matter 26, 126001 (2014).

16 H. H. Hng and L. Halim, Mater. Lett. 57, 1411 (2003).

17 M.-T. Dau, A. Spiesser, T. LeGiang, L. A. Michez, S. F. Olive-Mendez, V. Le Thanh, M. Petit, J.-M. Raimundo, A. Glachant, and J. Derrien, Thin Solid Films 518, S266 (2010).

18 H. Niida, T. Hori, H. Onodera, Y. Yamaguchi, and Y. Nakagawa, J. Appl. Phys. 79, 5946 (1996).

19 H. Kurt, N. Baadji, K. Rode, M. Venkatesan, P. Stamenov, S. Sanvito, and J. M. D. Coey, Appl. Phys. Lett. 101, 132410 (2012).

20 J. Winterlik, B. Balke, G. H. Fecher, and C. Felser, Phys. Rev. B 77, 054406 (2008).